AIAA JOURNAL
Vol. 36, No. 11, November 1998

Simulation of Dynamic Methane Jet Diffusion Flames Using Finite Rate Chemistry Models

Viswanath R. Katta[*]
Innovative Scientific Solutions, Inc., Dayton, Ohio 45440-3638
and
W. M. Roquemore[†]
U.S. Air Force Research Laboratory, Wright–Patterson Air Force Base, Ohio 45433-7103

Detailed calculations for methane jet diffusion flames under laminar and transitional conditions are made using an axisymmetric, time-dependent computational fluid dynamics code and different chemical-kinetics models. Comparisons are made with experimental data for a steady-state flame and for two dynamic flames that are dominated by buoyancy-driven instabilities. The ability of the three chemistry models—namely, 1) the modified Peters mechanism without C_2 chemistry, 2) the modified Peters mechanism with C_2 chemistry, and 3) the Gas Research Institute's Version 1.2 mechanism—in predicting the structure of coaxial jet diffusion flames under different operating conditions is investigated. It is found that the modified Peters mechanisms with and without C_2 chemistry are sufficient for the simulation of jet diffusion flames for a wide range of fuel-jet velocities. Detailed images of the vortical structures associated with the low- and transitional-speed methane jet flames are obtained using the reactive-Mie-scattering technique. These images suggest that a counter-rotating vortex is established upstream of the buoyancy-induced toroidal vortex in the low-speed-flame case and that the shear-layer vortices that develop in the transitional-speed flame are dissipated as they are convected downstream. The time-dependent calculations made using the modified Peters chemistry model have captured these unique features of the buoyancy-influenced jet flames. Finally, the unsteady flame structures obtained at a given height are compared with the steady-state flame structures.

Nomenclature

A = coefficient used in finite difference equation
A_k = pre-exponential in Arrhenius rate expression
c_p = specific heat of mixture
D_{im} = diffusion coefficient ith species in the mixture
E = activation energy
g = gravitational acceleration
H = enthalpy
h = total enthalpy
h_f^0 = heat of formation at standard state
Le = Lewis number
M = molecular weight
N_s = total number of species
p = pressure
R_0 = universal gas constant
r = radial distance
r_f = radius of flame surface
S^Φ = source term in Φ equation
T = temperature
t = time
u = axial-velocity component
v = radial-velocity component
X_i = mole fraction of ith species
Y_i = mass fraction of ith species
z = axial distance
α = constant appearing in modified Arrhenius rate expression
Γ^Φ = transport coefficient in Φ equation
λ = thermal conductivity
μ = viscosity
ρ = density
ρ_0 = density of air
Φ = flow variable
$\dot{\omega}$ = net rate of production of a species

Subscripts

i = ith species
P = reference grid point
z^+, r^+ = grid points adjacent to P in z and r directions, respectively
z^{++}, r^{++} = two grid points away from P in z and r directions, respectively
z^-, r^- = grid points adjacent to P in negative z and r directions, respectively
z^{--}, r^{--} = two grid points away from P in negative z and r directions, respectively

Superscripts

$N, N+1$ = time-step numbers

Introduction

INVESTIGATIONS of unsteady flames are important for understanding combustion phenomena in practical systems and for developing theories of turbulent-combustion processes. For this reason dynamic jet flames have been actively studied since the classic work of Hottel and Hawthorne[1] was published in 1949. Most of the data obtained in the past were on statistical quantities such as time-averaged and rms values of velocity, temperature, and species concentration, and point and planar measurement techniques were used. These data have formed the basis for understanding many of the processes occurring in dynamic jet diffusion flames. However, such understanding has limited applications for engineering problems because of the time-averaged description of the underlying unsteady combustion processes. In many cases, the mean and fluctuating quantities can mask the physics and chemistry that are germane to an understanding of the fundamental processes that give rise to the statistical results. This is particularly true for

---

Presented as Paper 97-0904 at the AIAA 35th Aerospace Sciences Meeting, Reno, NV, Jan. 6–9, 1997; received Sept. 12, 1997; revision received June 30, 1998; accepted for publication July 27, 1998.

[*] Senior Engineer, 2766 Indian Ripple Road. E-mail: vrkatta@snake.appl.wpafb.af.mil. Member AIAA.

[†] Senior Scientist, Propulsion Directorate. Member AIAA.

laminar and near-transitional jet flames in which the large-scale, low-frequency (0–40 Hz), organized buoyancy-induced vortices on the air side of the flame and medium-frequency (100–1000 Hz), Kelvin–Helmholtz-type vortex structures on the fuel side of the flame dominate the flame characteristics. For example, high-speed visualizations of a buoyant jet diffusion flame have revealed that the flame surface is actually wrinkled as a result of the interaction of vortices, whereas time-averaged visualizations indicate a smooth surface. To gain insight into these low- and medium-frequency dynamic processes, it is helpful—and, perhaps, essential—to think in terms of the time-dependent characteristics of jet flames.

Several past numerical investigations on dynamic jet flames employed conserved-scalar and primitive-variable approaches. These studies revealed important aspects of combustion such as the effect of heat-release rate,[2,3] the role of buoyancy,[4–6] the enhancement of soot formation,[7] and Lewis number effects.[8,9] However, in most of these studies a simple, one-step global-chemistry model was used for representing the combustion processes. On the other hand, studies incorporating finite rate chemistry are limited to hydrogen fuel because the kinetic models for this fuel are relatively simple. Because of the complex nature of hydrocarbon reaction mechanisms, detailed flame calculations for hydrocarbon fuels are restricted to steady-state problems.[10,11] However, for understanding processes such as flame stabilization,[12] local extinction,[13] and ignition[14] in dynamic hydrocarbon flames, these flames must be simulated with sufficiently accurate models for physical and chemical processes. Over the past five years, the authors have been developing time-accurate computational fluid dynamics with chemistry (CFDC) codes by incorporating different detailed chemical-kinetics models for the investigation of unsteady jet diffusion flames.[15–17] Studies employing these codes have indicated that consideration of finite rate chemistry is essential for the simulation of localized hot spots in temperature and species concentration on the wrinkled flame surfaces.[18]

The present paper describes a numerical study conducted using the CFDC code on a coaxial methane jet diffusion flame formed under different flow conditions. The accuracy of three detailed chemical-kinetics models [Peters mechanisms with and without C_2 chemistry and the Gas Research Institute's (GRI) Version 1.2 mechanism] in simulating a steady methane diffusion flame is assessed. The dynamic flames predicted by the CFDC code are compared with experimental flame images obtained using the reactive-Mie-scattering technique. Finally, the structure of the dynamic flame is compared with that of the steady-state flame to quantify the impact of vortex–flame interactions on jet flames.

Modeling

A time-dependent, axisymmetric mathematical model that solves for axial- and radial-momentum equations, continuity, and enthalpy- and species-conservation equations is used to simulate the dynamic jet diffusion flames. The governing equations, written in the cylindrical coordinate system, are as follows:

$$\frac{\partial \rho}{\partial t} + \frac{\partial \rho u}{\partial z} + \frac{1}{r}\frac{\partial (r\rho v)}{\partial r} = 0 \tag{1}$$

$$\frac{\partial(\rho\Phi)}{\partial t} + \frac{\partial(\rho u \Phi)}{\partial z} + \frac{1}{r}\frac{\partial(r\rho v\Phi)}{\partial r} = \frac{\partial}{\partial z}\left(\Gamma^{\Phi}\frac{\partial \Phi}{\partial z}\right) + \frac{1}{r}\frac{\partial}{\partial r}\left(r\Gamma^{\Phi}\frac{\partial \Phi}{\partial r}\right) + S^{\Phi} \tag{2}$$

The general form of Eq. (2) represents the momentum, the species, or the energy-conservation equation, depending on the variable used in place of Φ. The transport coefficients Γ^{Φ} and the source terms S^{Φ} that appear in the governing equations are given in Table 1. The body-force term due to the gravitational field is included in the axial-momentum equation, where $\dot{\omega}_i$ is the mass-production rate of the ith species, and ρ_0 is the density of air. The transport property D_{im} is calculated from the binary diffusion coefficients between the ith species and the other individual species. Finally, Le_i is the Lewis number of the ith species, which is defined as

$$Le_i \equiv \frac{\lambda}{\rho D_{im} c_p} \tag{3}$$

Table 1 Transport coefficients and source terms appearing in governing equations

Φ	Γ^{Φ}	S^{Φ}
u	μ	$-\frac{\partial p}{\partial z} + (\rho_0 - \rho)g + \frac{\partial}{\partial z}\left(\mu\frac{\partial u}{\partial z}\right) + \frac{\partial}{\partial r}\left(\mu\frac{\partial v}{\partial z}\right) + \frac{\mu}{r}\frac{\partial v}{\partial z} - \frac{2}{3}\left[\frac{\partial}{\partial z}\left(\mu\frac{\partial u}{\partial z}\right) + \frac{\partial}{\partial z}\left(\mu\frac{\partial v}{\partial r}\right)\right] + \frac{\partial}{\partial z}\left(\mu\frac{v}{r}\right)$
v	μ	$-\frac{\partial p}{\partial r} + \frac{\partial}{\partial z}\left(\mu\frac{\partial u}{\partial r}\right) + \frac{\partial}{\partial r}\left(\mu\frac{\partial v}{\partial r}\right) + \frac{\mu}{r}\frac{\partial v}{\partial r} - 2\mu\frac{v}{r^2} - \frac{2}{3}\left[\frac{\partial}{\partial r}\left(\mu\frac{\partial u}{\partial z}\right) + \frac{\partial}{\partial r}\left(\mu\frac{\partial v}{\partial r}\right)\right] + \frac{\partial}{\partial r}\left(\mu\frac{v}{r}\right)$
Y_i $(i = 1 - N_s - 1)$	ρD_{im}	$\dot{\omega}_i$
H	$\frac{\lambda}{c_p}$	$\nabla\left\{\frac{\lambda}{c_p}\sum_{1}^{N_s}[(Le^{-1} - 1)H_i\nabla Y_i]\right\} - \sum_{1}^{N_s}\left(h^0_{f_i}\dot{\omega}_i\right)$

The set of expressions given by Eqs. (1) and (2) can be completed using the global-species-conservation equation

$$Y_{N_s} = 1.0 - \sum_{i}^{N_s - 1} Y_i \tag{4}$$

and the state equation

$$p = \rho T R_0 \sum_{1}^{N}\left(\frac{Y_i}{M_i}\right) \tag{5}$$

Whereas the density is obtained by solving the state equation (4), the pressure field at every time step is determined from pressure Poisson equations. Even though the governing equations are solved in an uncoupled manner, the species-conservation equations are coupled through the source terms during the solution process to improve the stability of the algorithm. Such coupling is essential in finite rate chemistry calculations because the high-reaction-rate terms make the species-conservation equations quite stiff. Temperature- and species-dependent thermodynamic and transport properties are used in this formulation.

The governing equations for u and v momentum are integrated using an implicit quadratic upstream interpolation for convective kinematics with estimated streaming terms numerical scheme,[17,19] which is third order accurate in both space and time and has a very low numerical diffusion error. On the other hand, the finite difference form of the species and enthalpy is obtained using the hybrid scheme[20] with upwind and central differencing. An orthogonal, staggered-grid system with rapidly expanding cell sizes in both the z and the r directions is utilized for discretizing the governing equations. After rearrangement of terms, the finite difference form of the governing equation for the variable Φ at a grid point P can be written as an algebraic equation as follows:

$$\begin{aligned} A_P\Phi_P^{N+1} &+ A_{z^{++}}\Phi_{z^{++}}^{N+1} + A_{z^{+}}\Phi_{z^{+}}^{N+1} + A_{z^{-}}\Phi_{z^{-}}^{N+1} \\ &+ A_{z^{--}}\Phi_{z^{--}}^{N+1} + A_{r^{++}}\Phi_{r^{++}}^{N+1} + A_{r^{+}}\Phi_{r^{+}}^{N+1} \\ &+ A_{r^{-}}\Phi_{r^{-}}^{N+1} + A_{r^{--}}\Phi_{r^{--}}^{N+1} = S_P^{\Phi} + \Delta t \cdot \rho_P\Phi_P^{N} \end{aligned} \tag{6}$$

The time increment t is determined from the stability constraint and maintained as a constant during the entire calculation. The superscripts N and $N + 1$ represent the known variables at the Nth time step and the unknown variables at the $(N + 1)$th time step, respectively. The coefficients A and the terms on the right-hand side of the preceding equations are calculated from the known flow variables at the Nth time step. The preceding equations for $N_s + 2$ variables are solved individually using an iterative alternative direction implicit technique. The pressure field at every time step is accurately calculated by simultaneously solving the system of algebraic pressure

Poisson equations at all grid points using the lower-upper decomposition technique.

Three detailed chemical-kinetics models proposed in the literature for methane air combustion were used in this study. The first was proposed by Peters[21] and consists of 17 species (CH_4, O_2, CH_3, CH_2, CH, CH_2O, CHO, CO_2, CO, H_2, H, O, OH, H_2O, HO_2, H_2O_2, and N_2) that are involved in 52 elementary reactions. This mechanism is derived from the one originally published[21] for the hydrocarbon fuels up to propane in terms of carbon content and by neglecting the species that have more than one carbon element. The second chemistry model is an extension of the first and was obtained by including the C_2 chemistry,[21] which adds seven species (C_2H, C_2H_2, C_2H_3, C_2H_4, C_2H_5, C_2H_6, and CHCO) and 29 reactions. Finally, the third chemical-kinetics model, GRI Version 1.2, used in the present study was compiled by the Gas Research Institute. This is the most comprehensive mechanism, having 31 species and 346 elementary reaction steps, and is recommended by several investigators for computing the structures of methane flames.[22] In addition to the 24 species in the second model (Peters mechanism with C_2 chemistry), the GRI mechanism uses the following 7 species: C, $CH_2(S)$, CH_2OH, CH_3O, CH_3OH, CH_2CO, and HCCOH.

The enthalpies of all of the species are calculated from the polynomial curvefits developed for the temperature range 300–5000 K. Physical properties such as viscosity, thermal conductivity, and the binary molecular diffusion coefficients of the species are calculated using molecular dynamics. Mixture viscosity and thermal conductivity are then estimated using the Wilke and the Kee expressions,[23] respectively. Molecular diffusion is assumed to be of the binary type, and the diffusion velocity of a species is calculated according to Fick's law and using the effective-diffusion coefficient[24] of that species. The Lennard Jones potentials, the effective temperatures, and the coefficients for the enthalpy polynomials for each species are obtained from the CHEMKIN libraries.

The flowfield considered in the present study has vortical structures of two scales. Small-scale vortices develop on the fuel side of the flame surface along the shear layer of the fuel jet, and larger-scale vortices form on the air side of the flame surface. Unsteady axisymmetric calculations are made on a physical domain of 200 × 150 mm utilizing a 201 × 71 nonuniform grid system. Generally, the computational domain is bounded by the axis of symmetry and an outflow boundary in the radial direction and by the inflow and another outflow boundary in the axial direction. The outer boundaries in the z and r directions are located sufficiently far from the nozzle exit ($\sim$30 nozzle diameters) and the symmetry axis ($\sim$20 nozzle diameters), respectively, that propagation of boundary-induced disturbances into the region of interest is minimized. However, for the cases in which the flames were enclosed in a chimney, the outer boundary in the radial direction is located at a distance equal to the chimney radius, and no-slip wall conditions were imposed along this boundary.

Jet diffusion flames usually anchor to the outer edge of the burner lip, and the structure of the flame near the base depends on the boundary layer developed on the fuel tube and the heat transfer between the burner lip and the flame. However, at downstream locations (typically >1 burner diameter) the structure of the flame becomes insensitive to the flame-base conditions. Because the present study was focused on the region away from the flame base, flow in the neighborhood of the burner lip was not simulated. Flat velocity profiles were imposed at the fuel and air inflow boundaries to represent the flows exiting a contoured nozzle and a large annular duct, respectively. An extrapolation procedure with weighted zero- and first-order terms was used to estimate the flow variables at the outflow boundary.[25]

The simulations presented here were performed on a Pentium Pro 200-MHz-based personal computer with 128 MB of memory. Typical execution times using the modified Peters mechanisms without and with C_2 chemistry and the GRI Version 1.2 mechanism are $\sim$20, $\sim$40, and $\sim$100 s/time step, respectively. Stably oscillating flames are usually obtained in about 3000 time steps (which corresponds to approximately four flicker cycles), starting from the solution obtained with a global-chemistry model.[15,17] It is interesting to note that, for a transitional jet diffusion flame having vortices inside and outside the flame surface, a detailed time-dependent simulation using 31 species and 346 elementary reactions (GRI Version 1.2 mechanism) can be made on a personal computer in <80 h.

Results and Discussion

Because of the complex nature of chemical kinetics for methane combustion, several mechanisms with varying degrees of simplification have been proposed in the literature.[26–28] It is important to note that most of these mechanisms have been validated using well-stirred-reactor data (zero-dimensional problem) and counterflow flames (one-dimensional problem). However, because the multidimensional flames that are encountered in practical geometries are subjected to varying levels of strain rate, unsteadiness, and curvature, for example, a question arises as to the accuracy of the predictions of these chemistry models when used for multidimensional flame problems. Initially calculations were made for jet diffusion flames for several jet velocities using different chemical-kinetics models available in the literature. Indeed, our initial attempts to simulate jet diffusion flames with simpler chemistry models (such as in Ref. 26) resulted in unacceptable flame standoff distances (separation between the flame base and the nozzle exit) for different fuel jet velocities. The most recent skeletal mechanism proposed by Peters for methane combustion (24 species and 81 reactions) yielded well-attached flames for lower fuel jet velocities but failed to predict the flames that are formed at higher velocities. A trial-and-error investigation of this mechanism revealed that the methyl-radical recombination reaction ($CH_3 + H = CH_4$) is very sensitive to the extinction and standoff distance characteristics of diffusion flames. When the reaction rate proposed by Peters for this reaction is replaced by that proposed by Warnatz,[29] excellent agreement between experiment and calculation is obtained over a wide range of fuel and annular-air velocities. The mechanism obtained after replacing the rate data for the methyl-radical-recombination reaction is referred to as the modified Peters mechanism in this paper and is listed in Table 2. The reaction that differs from the original Peters mechanism is R45 in this table. Further details about the development of the modified Peters mechanism can be found in Ref. 30.

Steady-State Flame

The mathematical model and the numerical procedure used in the present investigation were tested for their accuracy in simulating a confined jet diffusion flame. The flame chosen for this purpose was previously studied experimentally by Mitchell et al.[31] and numerically by Smooke.[10] The burner assembly consists of a 12.7-mm-diam central fuel tube and a large 50.8-mm-diam coannular-air duct. The burner is enclosed in a 300-mm-long Pyrex® tube; therefore, the no-slip boundary condition is employed at the end of the computational domain in the radial direction. Pure methane is used as the fuel. The flow rates for the fuel and air are such that the velocities at the exits of the central fuel tube and the annular-air duct are 0.045 and 0.0988 m/s, respectively. The experimental data on this methane jet diffusion flame obtained by Mitchell et al.[31] suggest that the flame is in steady state; hence, Smooke[10] performed steady-state axisymmetric calculations for this flame. Gravitational force, which is quite significant in this low-speed flame, is considered in Smooke's steady-state calculations. Our previous studies on vertically mounted jet diffusion flames under similar velocity conditions indicated that buoyancy-driven vortical structures could develop and make the flame unsteady. However, the flame investigated by Mitchell et al.[31] was confined, and the ambient airflow into the flame was restricted, which could have suppressed the growth of the buoyancy-induced instabilities. For comparison purpose, unsteady calculations were performed for this flame using the code described previously and with the three different chemistry models. Interestingly, the computed flame established weak vortical structures outside the flame surface. As these vortices are convected downstream, their interaction with the flame makes it flicker. However, the oscillations (or unsteadiness) up to a height of 60 mm above the burner are quite weak. Calculations performed without the Pyrex enclosure, i.e., replacing the wall boundary with the free outflow boundary, yielded much stronger fluctuations, which also suggests that confinement reduces the flame flicker.

Calculations were initially made using different mesh systems to obtain grid-independent results. The modified Peters mechanism without C_2 chemistry was used in these calculations, and the results obtained with 141 × 61 and 251 × 91 mesh systems are shown in Fig. 1. In each mesh system, grid points are clustered in the

Table 2 Modified Peters mechanism for methane jet diffusion flames

Reaction		A_k, mole, cm^3, s	α	E, cal/mole
H_2/O_2 chain reactions				
(R01) $H + O_2 \Rightarrow OH + O$		2.00E+14	0.0	16,800
(R02) $OH + O \Rightarrow H + O_2$		1.57E+13	0.0	840
(R03) $O + H_2 \Rightarrow OH + H$		5.06E+04	2.67	6,280
(R04) $OH + H \Rightarrow O + H_2$		2.22E+04	2.67	4,370
(R05) $H_2 + OH \Rightarrow H_2O + H$		1.00E+08	1.60	3,300
(R06) $H_2O + H \Rightarrow H_2 + OH$		4.31E+08	1.60	18,270
(R07) $OH + OH \Rightarrow O + H_2O$		1.50E+09	1.14	100
(R08) $H_2O + O \Rightarrow OH + OH$		1.47E+10	1.14	17,000
H_2O formation and consumption				
(R09) $O_2 + H + M \Rightarrow HO_2 + M$		2.30E+18	−0.8	0
(R10) $HO_2 + M \Rightarrow O_2 + H + M$		3.19E+18	−0.8	46,680
(R11) $HO_2 + H \Rightarrow OH + OH$		1.50E+14	0.0	1,000
(R12) $HO_2 + H \Rightarrow H_2 + O_2$		2.50E+13	0.0	692
(R13) $HO_2 + OH \Rightarrow H_2O + O_2$		6.00E+13	0.0	0
(R14) $HO_2 + H \Rightarrow H_2O + O$		3.00E+13	0.0	1,720
(R15) $HO_2 + O \Rightarrow OH + O_2$		1.80E+13	0.0	−406
H_2O_2 formation and consumption				
(R16) $HO_2 + HO_2 \Rightarrow H_2O_2 + O_2$		2.50E+11	0.0	−1,240
(R17) $OH + OH + M \Rightarrow H_2O_2 + M$		3.25E+22	−2.0	0
(R18) $H_2O_2 + M \Rightarrow OH + OH + M$		1.69E+24	−2.0	48,330
(R19) $H_2O_2 + H \Rightarrow H_2O + OH$		1.00E+13	0.0	3,580
(R20) $H_2O_2 + OH \Rightarrow H_2O + HO_2$		5.40E+12	0.0	1,000
(R21) $H_2O + HO_2 \Rightarrow H_2O_2 + OH$		1.80E+13	0.0	32,190
Recombination reactions				
(R22) $H + H + M \Rightarrow H_2 + M$		1.80E+13	−1.0	0
(R23) $H + OH + M \Rightarrow H_2O + M$		2.20E+22	−2.0	0
(R24) $O + O + M \Rightarrow O_2 + M$		2.90E+17	−1.0	0
CO/CO_2 mechanism				
(R25) $CO + OH \Rightarrow CO_2 + H$		4.40E+06	1.5	−740
(R26) $CO_2 + H \Rightarrow CO + OH$		4.96E+08	1.5	21,440
CH consumption reactions				
(R27) $CH + O_2 \Rightarrow CHO + O$		3.00E+13	0.0	0
(R28) $CO_2 + CH \Rightarrow CHO + CO$		3.40E+12	0.0	692
CHO consumption reactions				
(R29) $CHO + H \Rightarrow CO + H_2$		2.00E+14	0.0	0
(R30) $CHO + OH \Rightarrow CO + H_2O$		1.00E+14	0.0	0
(R31) $CHO + O_2 \Rightarrow CO + HO_2$		3.00E+12	0.0	0
(R32) $CHO + M \Rightarrow CO + H + M$		7.10E+14	0.0	16,800
(R33) $H + CO + M \Rightarrow CHO + M$		1.14E+15	0.0	2,380
CH_2 consumption reactions				
(R34) $CH_2 + H \Rightarrow CH + H_2$		8.40E+09	1.5	335
(R35) $CH + H_2 \Rightarrow CH_2 + H$		5.83E+09	1.5	3,125
(R36) $CH_2 + O \Rightarrow CO + H + H$		8.00E+13	0.0	0
(R37) $CH_2 + O_2 \Rightarrow CO + OH + H$		6.50E+12	0.0	1,500
(R38) $CH_2 + O_2 \Rightarrow CO_2 + H + H$		6.50E+12	0.0	1,500
CH_2O consumption reactions				
(R39) $CH_2O + H \Rightarrow CHO + H_2$		2.50E+13	0.0	3,990
(R40) $CH_2O + O \Rightarrow CHO + OH$		3.50E+13	0.0	3,490
(R41) $CH_2O + OH \Rightarrow CHO + H_2O$		3.00E+13	0.0	1,200
(R42) $CH_2O + M \Rightarrow CHO + H + M$		1.40E+17	0.0	76,500
CH_3 consumption reactions				
(R43) $CH_3 + H \Rightarrow CH_2 + H_2$		1.80E+14	0.0	15,050
(R44) $CH_2 + H_2 \Rightarrow CH_3 + H$		3.68E+13	0.0	10,580
(R45) $CH_3 + H \Rightarrow CH_4$	K_∞	6.00E+16	−1.0	0
	K_0	8.00E+26	−3.0	0
(R46) $CH_3 + O \Rightarrow CH_2O + H$		7.00E+13	0.0	0
(R47) $CH_3 + CH_3 \Rightarrow C_2H_6$	K_∞	3.61E+13	0.0	0
	K_0	1.27E+41	−7.0	2,762
(R48) $CH_3 + O_2 \Rightarrow CH_2O + OH$		3.40E+11	0.0	8,940
(R49) $CH_3 + H_2 \Rightarrow CH_4 + H$		8.39E+02	3.0	8,260
(R50) $CH_3 + H_2O \Rightarrow CH_4 + OH$		2.63E+05	2.10	16,950
CH_4 consumption reactions				
(R51) $CH_4 + H \Rightarrow CH_3 + H_2$		2.20E+04	3.0	8,740
(R52) $CH_4 + O \Rightarrow CH_3 + OH$		1.20E+07	2.1	7,620
(R53) $CH_4 + OH \Rightarrow CH_3 + H_2O$		1.60E+06	2.1	2,460
C_2H consumption reactions				
(R54) $C_2H + H_2 \Rightarrow C_2H_2 + H$		1.10E+13	0.0	2,867
(R55) $C_2H_2 + H \Rightarrow C_2H + H_2$		5.27E+13	0.0	28,656
(R56) $C_2H + O_2 \Rightarrow CHCO + O$		5.00E+13	0.0	1,505
CHCO consumption reactions				
(R57) $CHCO + H \Rightarrow CH_2 + CO$		3.00E+13	0.0	0
(R58) $CH_2 + CO \Rightarrow CHCO + H$		2.36E+12	0.0	−7,021
(R59) $CHCO + O \Rightarrow CO + CO + H$		1.00E+14	0.0	0
C_2H_2 consumption reactions				
(R60) $C_2H_2 + O \Rightarrow CH_2 + CO$		4.10E+08	1.5	1,696
(R61) $C_2H_2 + O \Rightarrow CHCO + H$		4.30E+14	0.0	12,112
(R62) $C_2H_2 + OH \Rightarrow C_2H + H_2O$		1.00E+13	0.0	7,000
(R63) $C_2H + H_2O \Rightarrow C_2H_2 + OH$		9.00E+12	0.0	−3,818
C_2H_3 consumption reactions				
(R64) $C_2H_3 + H \Rightarrow C_2H_2 + H_2$		3.00E+13	0.0	0
(R65) $C_2H_3 + O_2 \Rightarrow C_2H_2 + HO_2$		5.40E+11	0.0	0
(R66) $C_2H_3 \Rightarrow C_2H_2 + H$	K_∞	2.00E+14	0.0	39,717
	K_0	1.19E+42	−7.5	45,486
(R67) $C_2H_2 + H \Rightarrow C_2H_3$	K_∞	1.05E+14	0.0	810
C_2H_4 consumption reactions				
(R68) $C_2H_4 + H \Rightarrow C_2H_3 + H_2$		1.50E+14	0.0	10,201
(R69) $C_2H_3 + H_2 \Rightarrow C_2H_4 + H$		9.61E+12	0.0	7,800
(R70) $C_2H_4 + O \Rightarrow CH_3 + CO + H$		1.60E+09	1.2	741
(R71) $C_2H_4 + OH \Rightarrow C_2H_3 + H_2O$		3.00E+13	0.0	3,010
(R72) $C_2H_3 + H_2O \Rightarrow C_2H_4 + OH$		8.29E+12	0.0	15,576
(R73) $C_2H_4 + M \Rightarrow C_2H_2 + H_2 + M$		2.50E+17	0.0	76,400
C_2H_5 consumption reactions				
(R74) $C_2H_5 + H \Rightarrow CH_3 + CH_3$		3.00E+13	0.0	0.0
(R75) $CH_3 + CH_3 \Rightarrow C_2H_5 + H$		3.57E+12	0.0	11,870
(R76) $C_2H_5 + O_2 \Rightarrow C_2H_4 + HO_2$		2.00E+12	0.0	4,993
(R77) $C_2H_5 \Rightarrow C_2H_4 + H$	K_∞	2.00E+13	0.0	39,657
	K_0	1.00E+17	0.0	31,057
(R78) $C_2H_4 + H \Rightarrow C_2H_5$	K_∞	3.19E+13	0.0	3,013
C_2H_6 consumption reactions				
(R79) $C_2H_6 + H \Rightarrow C_2H_5 + H_2$		5.40E+02	3.5	5,208
(R80) $C_2H_6 + O \Rightarrow C_2H_5 + OH$		3.00E+07	2.0	5,112
(R81) $C_2H_6 + OH \Rightarrow C_2H_5 + H_2O$		6.30E+06	2.0	645

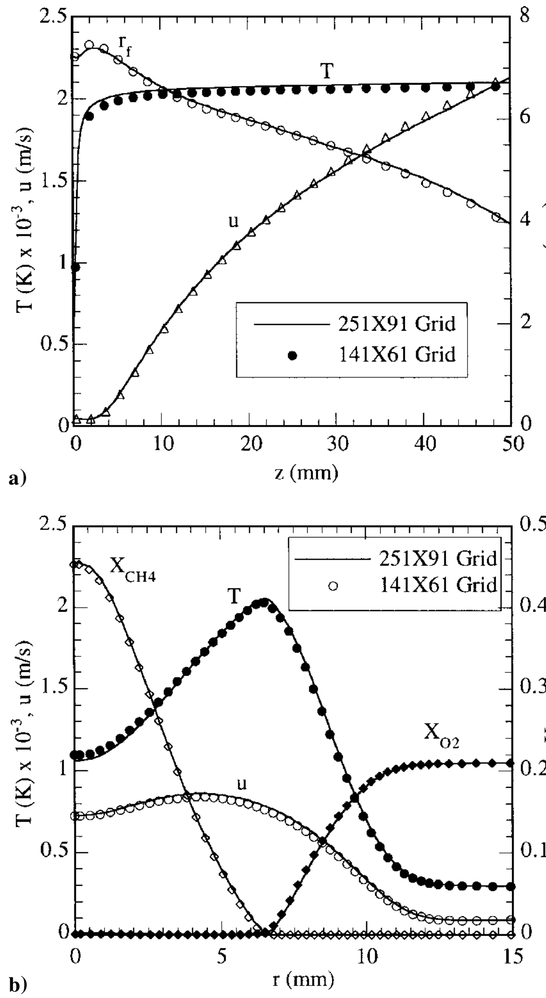

Fig. 1 Flame structures obtained with two different grids; calculations made using modified Peters mechanism without C_2 chemistry: a) axial distributions of peak temperature and its location and local axial velocity; and b) radial distributions of temperature, axial velocity, and fuel and oxygen mole fractions at z = 12 mm.

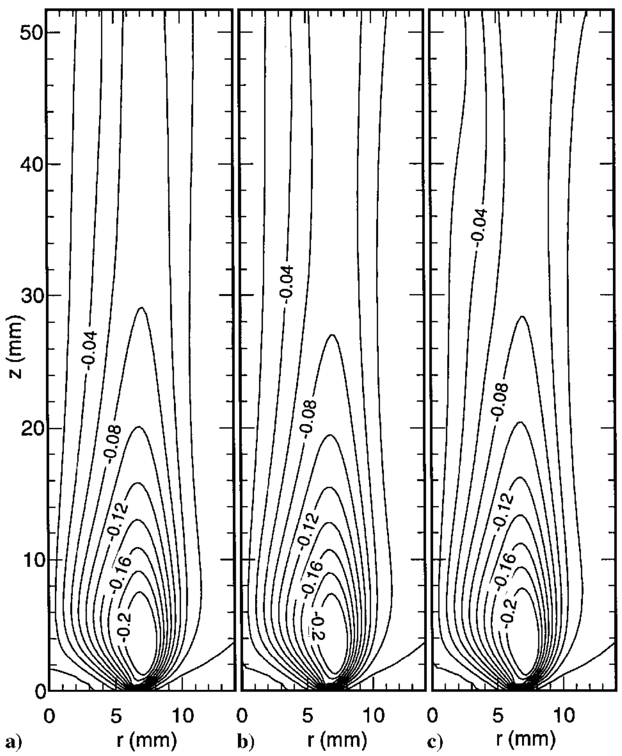

Fig. 2 Comparison of radial-velocity distributions obtained with a) modified Peters mechanism without C_2 chemistry, b) modified Peters mechanism with C_2 chemistry, and c) GRI Version 1.2 mechanism.

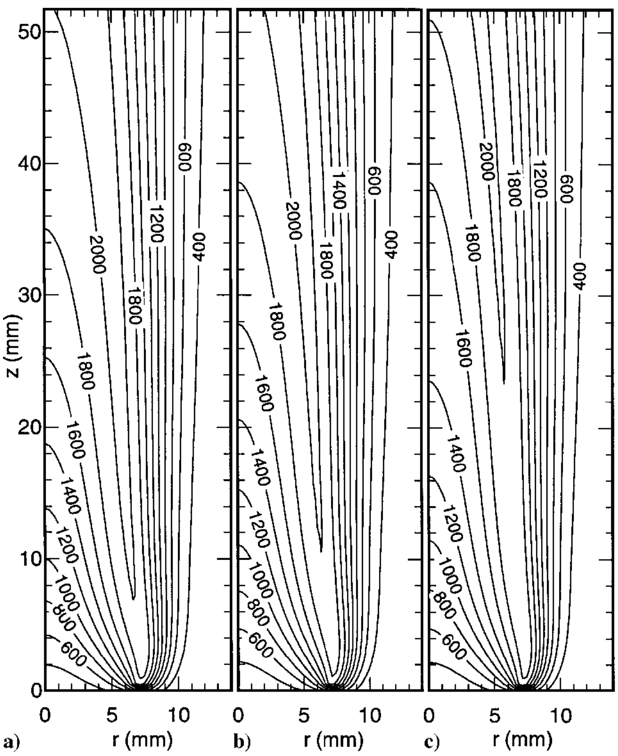

Fig. 3 Temperature distributions obtained with a) modified Peters mechanism without C_2 chemistry, b) modified Peters mechanism with C_2 chemistry, and c) GRI Version 1.2 mechanism.

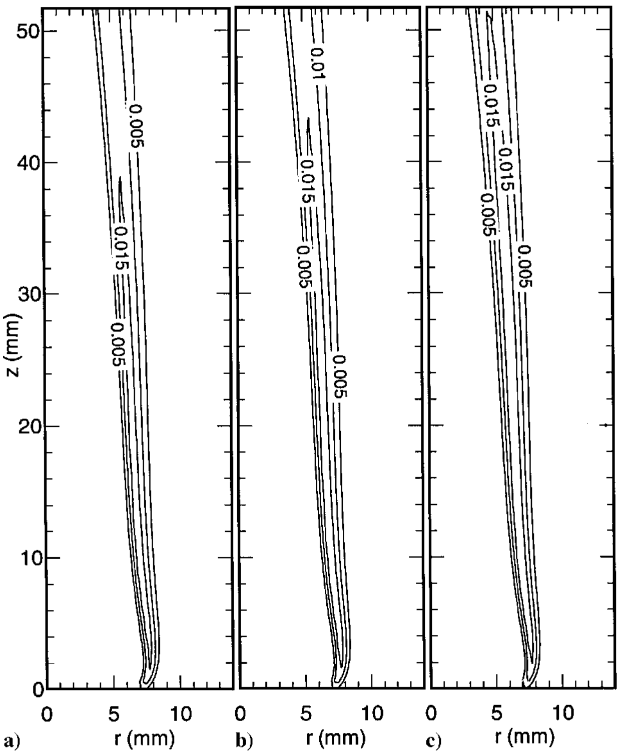

Fig. 4 OH-radical mole-fraction distributions obtained with a) modified Peters mechanism without C_2 chemistry, b) modified Peters mechanism with C_2 chemistry, and c) GRI Version 1.2 mechanism.

neighborhood of the flame zone located between 0 and 50 mm in the axial direction. Such clustering yielded grid spacings of 0.56 and 0.28 mm in the axial and radial directions, respectively, in the neighborhood of the flame zone with the 171 × 61 mesh. The corresponding grid spacings obtained with the 251 × 91 mesh system were 0.28 and 0.14 mm in the axial and radial directions, respectively.

The variation of peak temperature location r_f with axial distance in Fig. 1a suggests that the flame near the base is bulging outwardly to accommodate a weak recirculation zone in the fuel jet. In low-speed diffusion flames, acceleration of hot combustion products due to gravitational force leads to the formation of a recirculation zone in the fuel jet,[32] as seen in the axial-velocity distribution in Fig. 1a. A comparison of results in Fig. 1 obtained with 141 × 61 and 251 × 91 mesh systems suggests that the former mesh is yielding near-grid-independent results. A maximum difference of 24 K may be noted between the peak temperatures obtained with these two mesh systems. Based on these comparisons, further calculations for this flame were made using different chemistry mechanisms on a 141 × 71 mesh system.

The results in the form of isocontours of radial velocity, temperature, and mole fractions of CH_3 and OH radicals are shown in Figs. 2–5, respectively. The flowfields computed with the three chemistry models—namely, the modified Peters mechanism without C_2 chemistry (Fig. 2a), the modified Peters mechanism with C_2 chemistry (Fig. 2b), and the GRI Version 1.2 mechanism (Fig. 2c)—are quite similar. Weak oscillations resulting from the buoyancy-induced instability are evident from the slightly squeezed isoradial contours in the region between $z = 30$ and 50 mm.

All three chemistry models predicted the same temperature distributions (Fig. 3) on the air side of the flame ($r > 6.5$ mm). However, on the fuel side, the GRI mechanism predicted lower temperatures than the two modified Peters mechanisms. In fact, the peak temperature of 2040 K predicted by GRI chemical kinetics is 50 K lower than that obtained with the Peters mechanism without C_2 chemistry and ~20 K lower than that obtained with C_2 chemistry. These results suggest that the formation of higher hydrocarbons affects the flame structure on the fuel side of a jet diffusion flame. This is also evident in the methyl-radical-concentration plots of Fig. 5. Here, CH_3 is confined to the fuel side, and inclusion of C_2 chemistry reduces its concentration (compare Figs. 5a and 5b). The peak concentration for CH_3 radicals predicted by the Peters mechanism with C_2 chemistry (~0.006) is very near that predicted with the GRI Version 1.2 mechanism. Interestingly, the three kinetics models yielded similar distributions for OH-radical concentration (Fig. 4). As expected, the location of the peak OH concentration is found to be shifted from the peak temperature location and is on the air side.

The model predictions are compared with the measured values of Mitchell et al.[31] in Figs. 6–9. In each figure the data collected at three

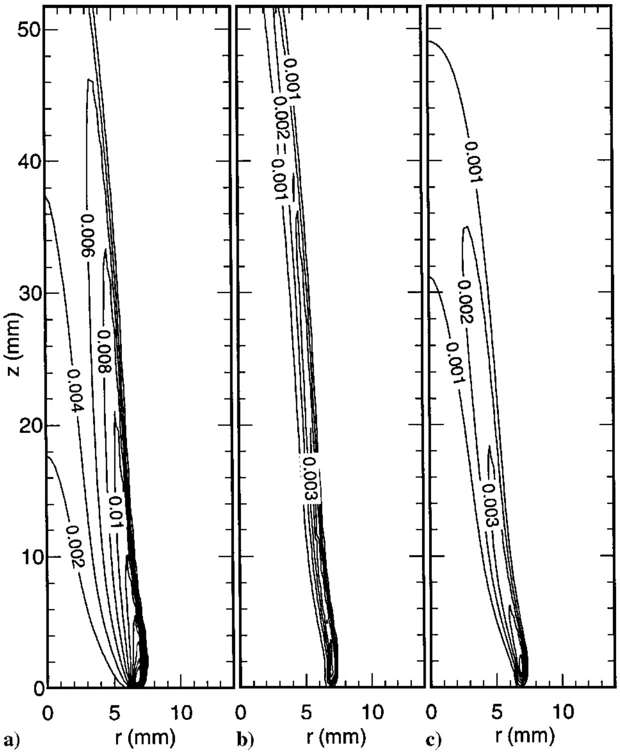

Fig. 5 Computed methyl-radical (CH_3) distributions with a) modified Peters mechanism without C_2 chemistry, b) modified Peters mechanism with C_2 chemistry, and c) GRI Version 1.2 mechanism.

heights, $z = 12$, 24, and 50 mm, are compared. Figure 6 compares temperature and axial velocity, and Figs. 7–9 show comparisons for species concentrations.

The experiments of Mitchell et al.[31] indicate that a noticeable amount of oxygen is present in the potential core of the flame at $z = 12$ mm (Fig. 7a). Calculations made with the Peters mechanism with C_2 chemistry and the GRI mechanism have reasonably predicted this feature of the diffusion flame. The decrease in measured oxygen concentration with radial distance in the potential core suggests that the observed oxygen on the fuel side of the flame was transported from upstream locations. However, for this to occur, the flame at the base (or burner exit) would not be completely attached to the burner such that oxygen would enter the potential core through the dark space between the flame base and the burner. The computed temperature distribution (obtained with the modified Peters without C_2 chemistry) plotted in Fig. 3a indicates that this flame is nearer to the nozzle than the other two flames (Figs. 3b and 3c), which, in turn, leads to lower oxygen concentration in the potential core in Fig. 7a. Because the standoff distance between the nozzle exit and the flame base depends on the heat transfer to the burner and on the nozzle geometry, which were not modeled in the present study, one should not conclude—based on the oxygen data in the fuel jet—that one mechanism is more accurate than the other.

Considering the limitations of the present CFDC model and the uncertainty in the experimental data, it may be concluded that all three chemical mechanisms are yielding reasonably accurate flame structures. However, because of the higher number of species and reaction steps, calculations with the GRI mechanism (31 species and 346 reaction) required a CPU time greater by a factor of 5 than that required for the calculations made with the Peters mechanism (17 species and 52 reactions) and greater by a factor of 3 than that required for the Peters mechanism with C_2 chemistry (24 species and 81 reactions).

Dynamic Flames

The experimental setup used for the study of these flames consists of vertically mounted coannular jets and is described in Ref. 33. The central fuel jet is a 25.4-mm-diam tube that contracts to a 10-mm-diam nozzle. The nozzle is designed to provide a flat mean velocity profile with low-velocity fluctuations at the nozzle exit. The annular-air jet has a diameter of 245 mm. An air velocity of 15 cm/s is used to reduce the room air disturbances in the first 15 diameters of the jet exit without significantly affecting the visible flame structure. Two flames were investigated experimentally and numerically. The first had a fuel-jet velocity of 0.5 m/s, and the second had a velocity of 4.1 m/s. Because of the buoyancy forces and the shear layer instability, these flames became dynamically oscillating ones.

Calculations for these flames were made using the three chemistry mechanisms described earlier. It was found that the global flame structures (i.e., the flame shapes, heights, and fluctuation frequencies) predicted by the three chemistry mechanisms were identical and that the chemical structures differed only on the fuel side of the flame zone where C_2 chemistry has some effect. For the sake of brevity, results obtained with the Peters mechanism with C_2 chemistry will be used in subsequent discussions of these dynamic flames.

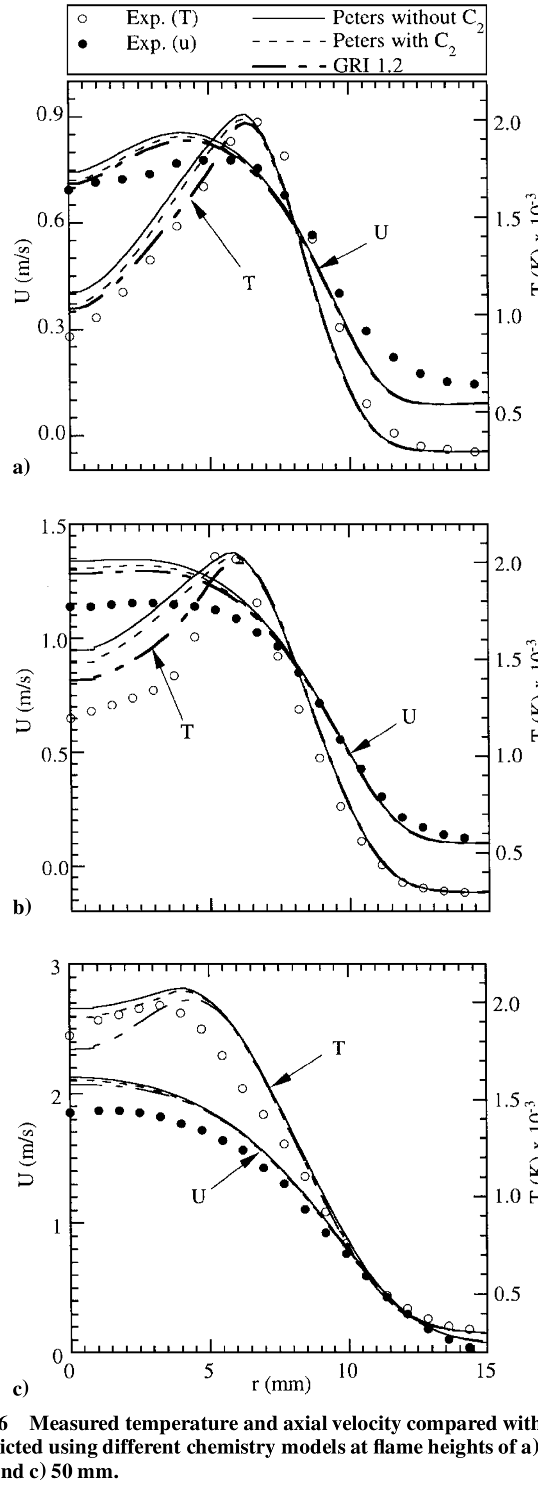

Fig. 6 Measured temperature and axial velocity compared with those predicted using different chemistry models at flame heights of a) 12, b) 24, and c) 50 mm.

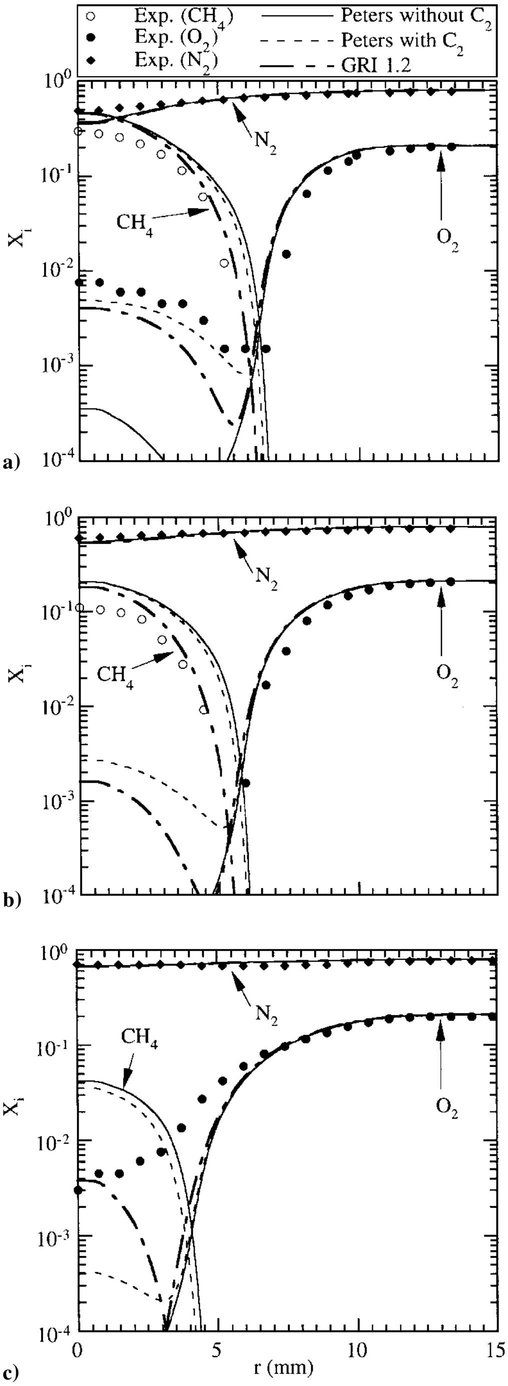

Fig. 7 CH_4, O_2, and N_2 concentrations predicted using different chemistry models compared with those measured at heights of a) 12, b) 24, and c) 50 mm.

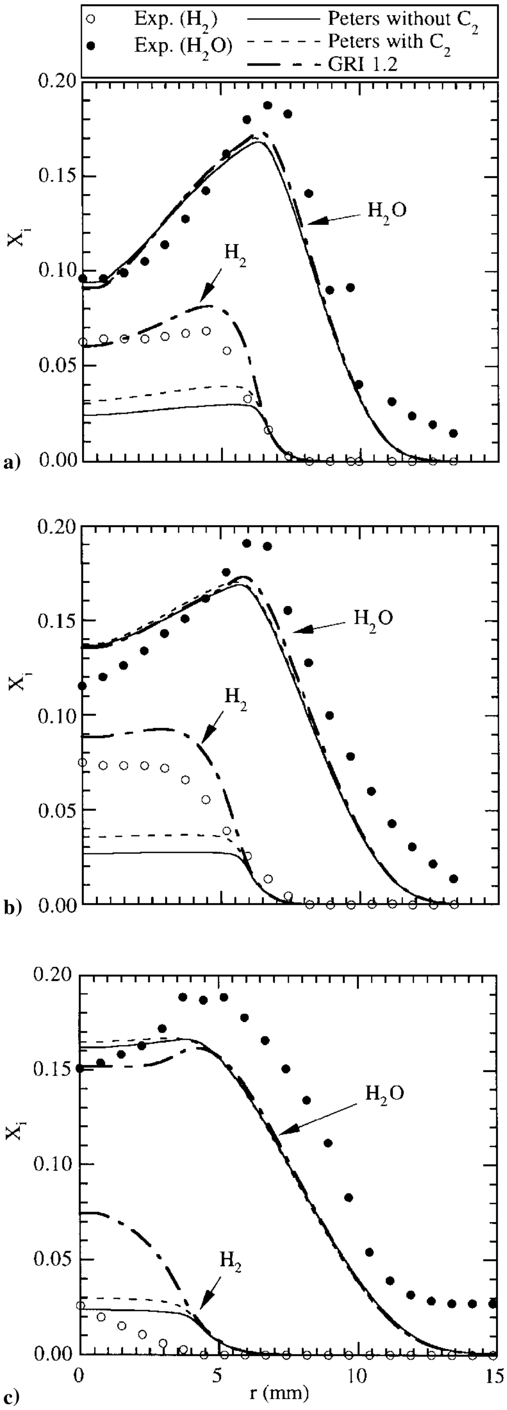

Fig. 8 H_2 and H concentrations predicted using different chemistry models compared with those measured at heights of a) 12, b) 24, and c) 50 mm.

An instantaneous image of the low-speed flame (fuel-jet velocity of 0.5 m/s) obtained with the reactive-Mie-scattering (RMS) technique[33] is shown in Fig. 10a. With this method micron-sized TiO_2 particles, formed from the spontaneous reaction between the seeded-$TiCl_4$ vapor and the water vapor produced during combustion, are visualized by the Mie-scattered light from a laser sheet. $TiCl_4$ is seeded into both the fuel and the annular-air flows. The bright region sandwiched between the inner and outer jets in Fig. 10a is the luminous flame surface captured simultaneously with the Mie-scattered light.

Because of the gravity term in the axial-momentum equation and the low-speed annular-air flow (~0.15 m/s), solution of the governing equations resulted in a dynamic flame, with large toroidal vortices forming naturally outside the flame surface. The computed instantaneous temperature field is shown in Fig. 10b. The flame (or peak temperature) surface that is identified from the temperature field is also shown (white solid circles). Note that no artificial perturbation is required for the formation of the outer vortices. In the presence of gravitational force, acceleration of hot gases along the flame surface generated the outer structures as part of the solution. As these vortices are convected downstream, they cause the flame to squeeze at certain locations ($z = 80$ and 160 mm) and bulge at others ($z = 50$ and 120 mm). The frequency corresponding to the passage of these outer vortices (also known as the flame-flickering frequency) is ~12 Hz. The instantaneous locations of the particles that are released along with the fuel are also shown (bright region in the center). The predicted flame structure compares extremely well with that obtained in experiments using the RMS technique. The counter-rotating toroidal vortex (at $z = 140$ mm in Fig. 10) that is formed as a result of the strong rotation of the upstream buoyancy-induced vortex[34] is accurately captured by the model.

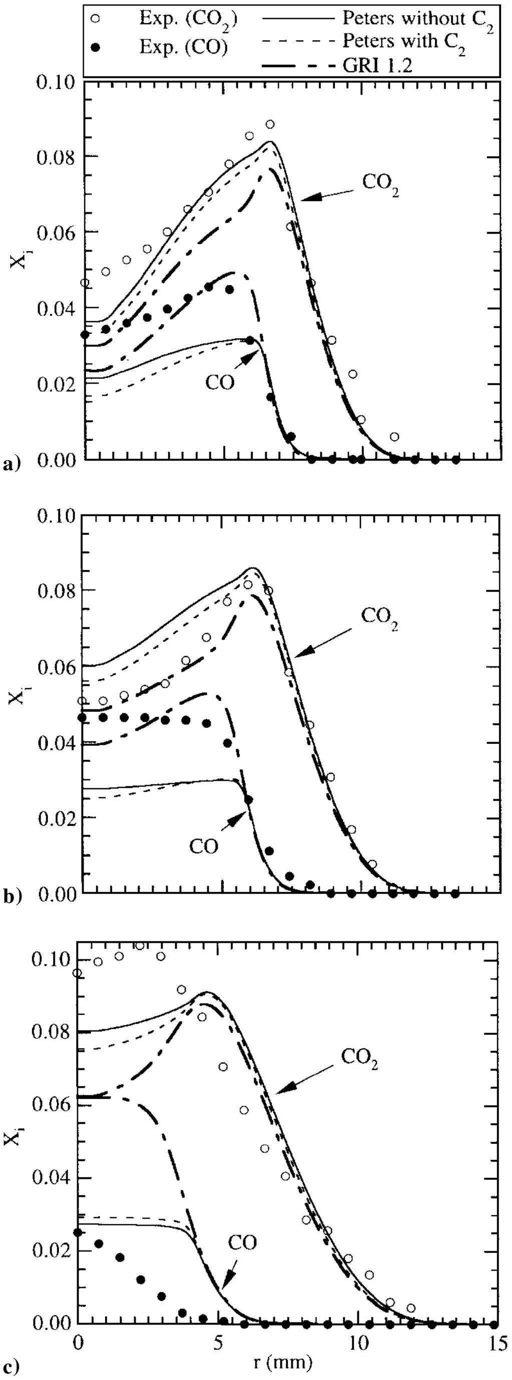

Fig. 9 CO_2 and CO concentrations predicted using different chemistry models compared with those measured at heights of a) 12, b) 24, and c) 50 mm.

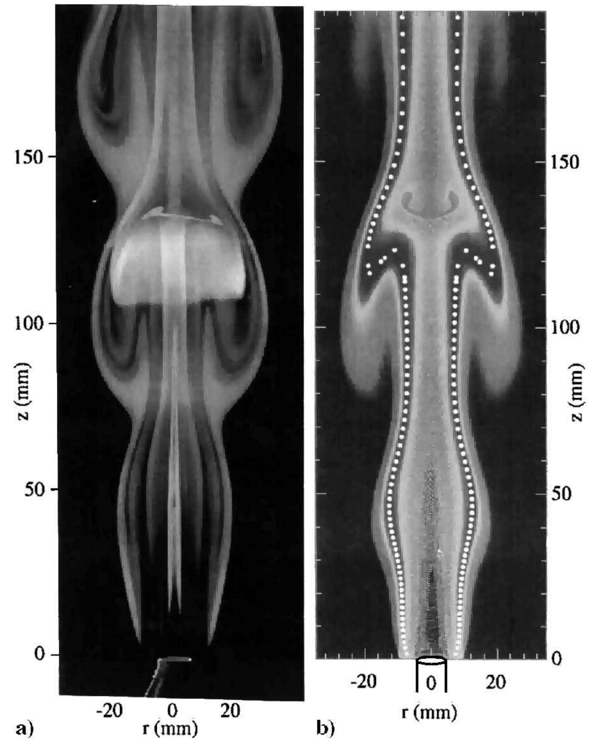

Fig. 10 Instantaneous images of experimental and computed low-speed dynamic flames. Fuel and air jet velocities are 0.5 and 0.15 m/s, respectively: a) RMS image showing naturally formed vortical structures and soot surface (bright region between the inner and outer jets); and b) locations of particles (bright central region) superimposed on computed temperature field. White solid circles represent high-temperature surface.

The instantaneous flame structure obtained for the higher (or transitional) fuel-jet-velocity case is compared with the RMS image of the experimental flame in Fig. 11. As expected, buoyancy-driven vortical structures have formed outside the flame surface in this case also, and the convective frequency for these structures is found to be ~13 Hz. Interestingly, the experimental flame has vortical structures inside as well as outside the flame zone. Initial calculations of this flame yielded only outer structures. The inner shear layer was very laminar in nature, having no structures. The inner vortices observed in the experiments (Fig. 11a) are thought to result from the small perturbations that are inherent in the high-speed jet flow and the Kelvin–Helmholz instability of the shear layer. Although the outer vortices in the calculations caused the jet shear layer to oscillate, even at the fuel nozzle exit, this low-frequency disturbance was not amplified in the jet shear layer and, thus, did not stimulate the growth of the small-scale structures.

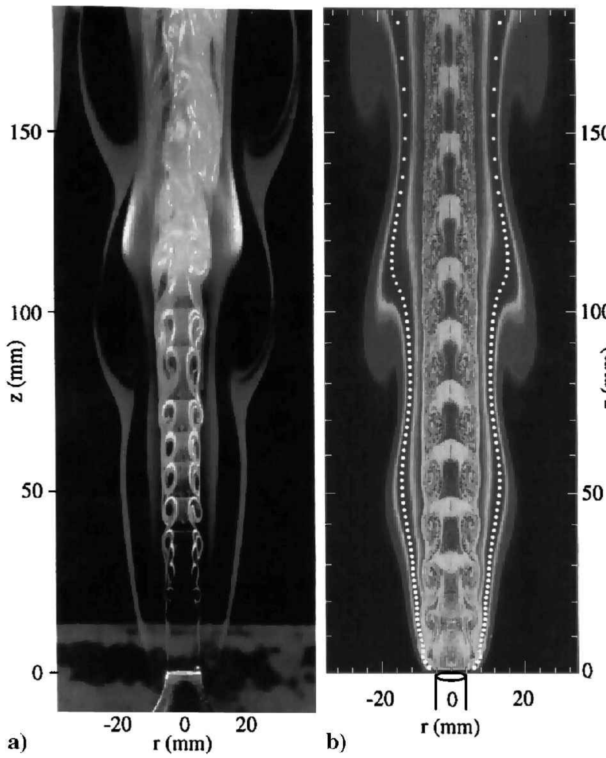

Fig. 11 Instantaneous images of experimental and computed transitional-speed dynamic flame. Fuel and air-jet velocities are 4.1 and 0.15 m/s, respectively: a) RMS image showing outer and inner vortices and soot surface (bright region between the inner and outer jets); and b) locations of particles (bright central region) superimposed on computed temperature field. White solid circles represent high-temperature surface.

To initiate and to sustain the Kelvin–Helmholtz instabilities in the calculations, constant external forcing in the form of background random noise (3% of jet velocity) was used at the exit of the fuel jet. The resulting flame is shown in Fig. 11b. The inner vortical structures are found to grow slowly and maintain their identities over a long distance. At locations farther downstream, these vortices dissipate with the entrainment of viscous combustion products from the flame surface.

In both the low- and transitional-speed flames (Figs. 10 and 11, respectively), it should be noted that the convective motion of the outer vortices interacts with the flame surface, making it wrinkle. These interactions perturb not only the shape but also the chemical structure of the flame. To illustrate the effects of vortex–flame interactions on flame structure, scatter plots of temperature and species concentration are shown in Figs. 12a and 12b for the steady-state flame, in Figs. 13a and 13b for the low-speed dynamic flame, and in Figs. 14a and 14b for the transitional-speed flame. The scatter plots for the dynamic flames (Figs. 13 and 14) were constructed by collecting 3000 instantaneous radial distributions that represent approximately four flickering cycles at a height of 80 mm above the burner. On the other hand, scatter plots for the steady-state flame (Fig. 12) were constructed from the data obtained along the radial lines at several flame heights in the region between $z = 2$ and 50 mm. Flame structures very near the burner ($z < 2$ mm) were discarded to avoid ambiguity that might result from inaccuracies in modeling the burner lip. Finally, the radial distributions were converted into mixture fraction ξ coordinates. Here, mixture fraction (ξ) is defined as the fraction of the mass at any location that originated from the fuel jet and is calculated from the following expression[35]:

$$\begin{aligned}\xi = 16.0[&X_{CH_4} + X_{CH_3} + X_{CH_2} + X_{CH} + X_{CH_2O} + X_{CHO} \\ &+ X_{CO_2} + X_{CO} + 0.5(X_{C_2H} + X_{C_2H_2} + X_{C_2H_3} + X_{C_2H_4} \\ &+ X_{C_2H_5} + X_{C_2H_6} + X_{CHCO} + X_{C} + X_{CH_2(S)} + X_{CH_2OH} \\ &+ X_{CH_3O} + X_{CH_3OH} + X_{CH_2CO} + X_{HCCOH})]\end{aligned}$$

where $X_i = Y_i/M_i/(Y_i/M_i)$.

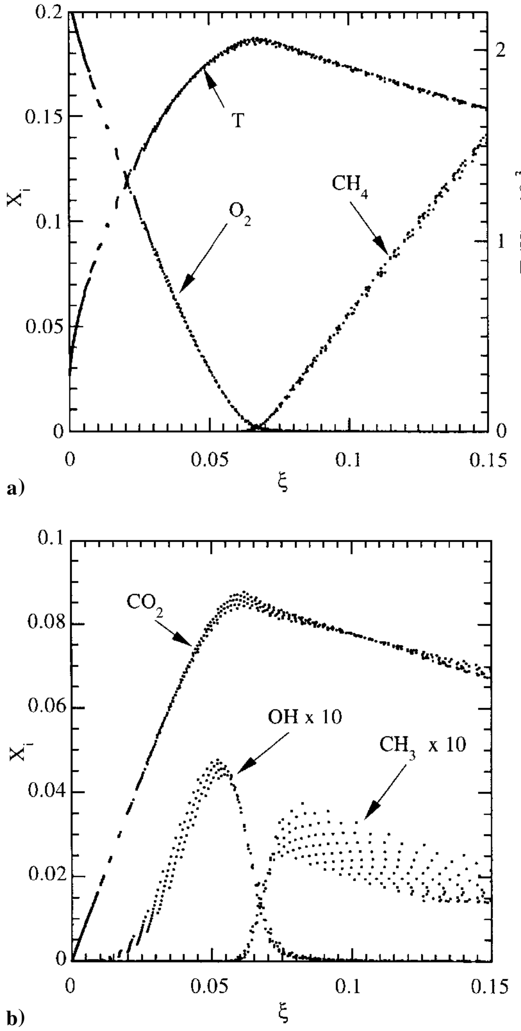

Fig. 12 Structure of steady-state flame constructed from radial distributions obtained at several heights: a) temperature and fuel and oxidizer concentrations with respect to mixture fraction; and b) variation of CO_2, CH_3, and OH concentration with respect to mixture fraction.

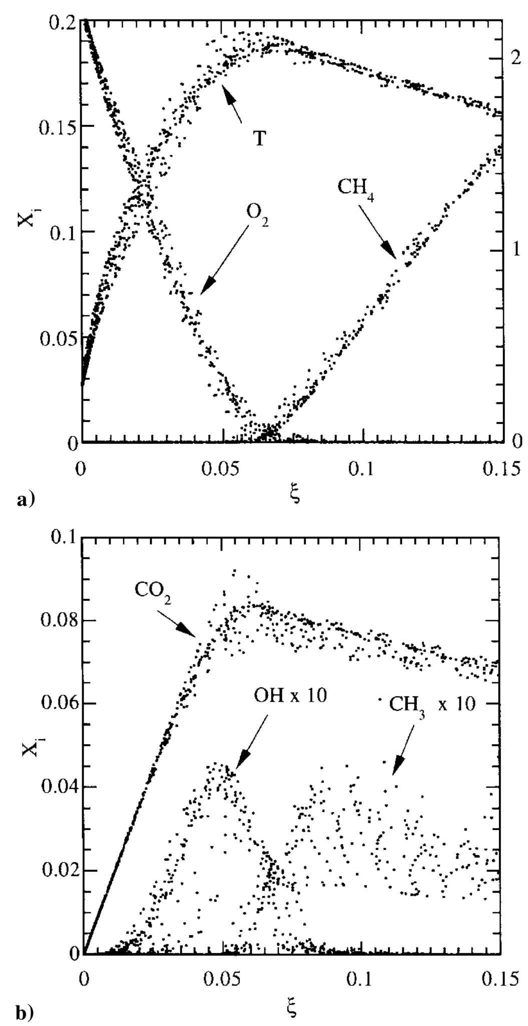

Fig. 13 Structure of low-speed buoyancy-influenced flame constructed at $z = 80$ mm from radial distributions obtained at several instants: a) temperature and fuel and oxidizer concentrations with respect to mixture fraction; and b) variation of CO_2, CH_3, and OH concentration with respect to mixture fraction.

In general, for a steady-state flame, the temperature, fuel concentration, and oxygen concentration yield self-similar solutions in the mixture fraction domain. However, this is not the case with respect to the intermediate species that are generated in the flame zone (cf. Fig. 12b). It is thought that the finite rate chemistry in combination with the varying convective velocities at different flame heights causes the species distributions to depend not only on mixture fraction but also on flame height. These deviations occur mainly for CH_3 on the fuel side ($\xi > 0.055$) and for OH radicals on the air side ($\xi < 0.055$) because these species are, in general, produced on the respective sides of the flame.

Vortex–flame interactions in the two dynamic flames resulted in scattered data for every variable shown in Figs. 13 and 14. Flame temperature increases at certain phases of the interaction (when the flame is compressed) and decreases at others (when the flame is stretched). These results are similar to those obtained for hydrogen

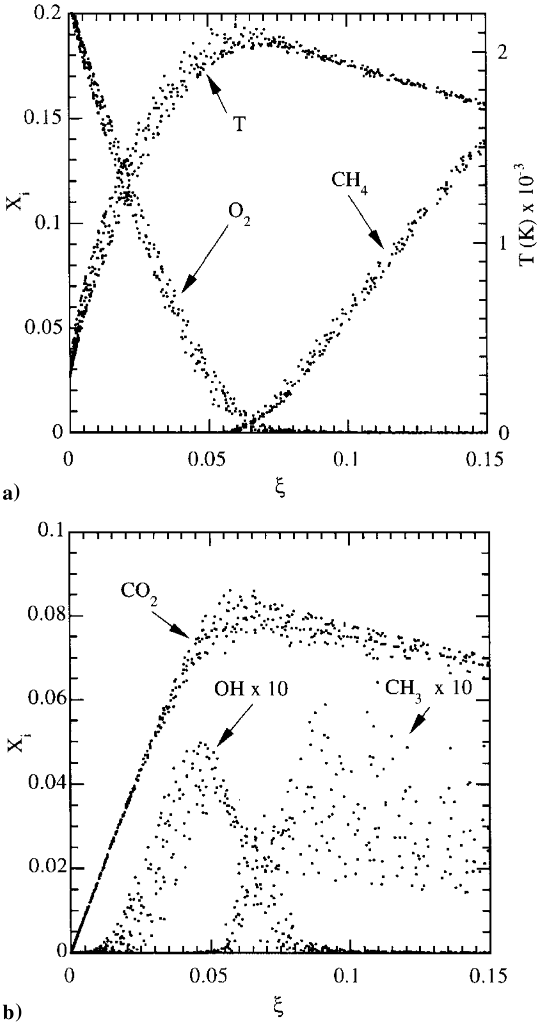

Fig. 14 Structure of a transitional-speed buoyancy-influenced flame constructed at $z = 80$ mm from radial distributions obtained at several instants: a) temperature and fuel and oxidizer concentrations with respect to mixture fraction; and b) variation of CO_2, CH_3, and OH concentration with respect to mixture fraction.

jet diffusion flames[8, 18] in which nonunity Lewis numbers were found to be responsible for such behavior. Because the Lewis number of methane is less than unity (similar to that of hydrogen), one might expect hydrogen and methane flames to behave similarly during vortex–flame interactions. Because the inner vortices in transitional-speed flames are not quite near the flame surface, their impact on the flame structure is evident neither in temperature nor in major species concentration. However, because CH_3 is produced mostly on the fuel side, these inner vortices cause more scatter in its concentration (Fig. 14b).

Conclusions

Accurate dynamic simulations employing detailed chemical-kinetics models for hydrocarbon fuels are needed for understanding flame structure and various processes involved in laminar and transitional jet flames. An axisymmetric, time-dependent CFDC code was developed for the simulation of methane jet diffusion flames. Calculations were performed for a steady-state flame and for two dynamic flames that have been investigated experimentally in the past. Three chemistry models—namely, 1) the modified Peters mechanism without C_2 chemistry, 2) the modified Peters mechanism with C_2 chemistry, and 3) the GRI Version 1.2 mechanism—were used in the simulations. It was found that the modified Peters mechanisms with and without C_2 chemistry are sufficient for the simulation of these jet diffusion flames. The predicted flame shapes and flow structures of the periodically oscillating flames that are dynamic as a result of buoyancy-induced instabilities showed good correlation with the RMS images of the flames obtained in experiments. Based on the scatter plots constructed from the data collected at several heights in the steady-state flame, it was found that temperature as well as fuel and oxygen concentrations collapse onto a single curve in the mixture fraction coordinates, whereas the intermediate species concentrations do not. It was also found that the temperature in buoyancy-dominated unsteady methane flames increases at certain phases of the vortex–flame interaction—behavior that is similar to that observed in a hydrogen flame.

Acknowledgments

This work was supported, in part, by Air Force Contract F33615-95-C-2507 and the U.S. Air Force Office of Scientific Research.

References

[1] Hottel, H. C., and Hawthorne, W. R., "Diffusion in Laminar Flame Jets," *Proceedings of Third Symposium (International) on Combustion, Flame and Explosive Phenomena*, Combustion Inst., Pittsburgh, PA, 1949, pp. 254–266.

[2] Ellzey, J. L., Laskey, K. J., and Oran, E. S., "Dynamics of an Unsteady Diffusion Flame: Effects of Heat Release Rate and Viscosity," *Dynamics of Deflagrations and Reactive Systems: Flames*, edited by A. L. Kahl, J. C. Leyer, A. A. Borisov, and W. A. Sirgnano, Vol. 131, Progress in Astronautics and Aeronautics, AIAA, Washington, DC, 1989, p. 179.

[3] Yamashita, H., Kushida, G., and Takeno, T., "A Numerical Study of the Transition of Jet Diffusion Flames," *Proceedings of the Royal Society of London A*, Vol. 431, No. 1882, 1990, pp. 301–314.

[4] Davis, R. W., Moore, E. F., Roquemore, W. M., Chen, L.-D., Vilimpoc, V., and Goss, L. P., "Preliminary Results of a Numerical-Experimental Study of the Dynamic Structure of a Buoyant Jet Diffusion Flame," *Combustion and Flame*, Vol. 83, No. 3/4, 1991, pp. 263–270.

[5] Katta, V. R., Goss, L. P., and Roquemore, W. M., "Effect of Nonunity Lewis Number and Finite-Rate Chemistry on the Dynamics of a Hydrogen-Air Jet Diffusion Flame," *Combustion and Flame*, Vol. 96, No. 1/2, 1994, pp. 60–74.

[6] Patnaik, G., and Kailasanath, K., "Numerical Simulations of Burner-Stabilized Hydrogen-Air Flames in Microgravity," *Combustion and Flame*, Vol. 99, No. 10, 1994, pp. 247–253.

[7] Kaplan, C. R., Oran, E. S., Kailasanath, K., and Ross, H. D., "Gravitational Effects on Sooting Diffusion Flames," *26th Symposium (International) on Combustion*, Combustion Inst., Pittsburgh, PA, 1996, pp. 1301–1309.

[8] Katta, V. R., Goss, L. P., and Roquemore, W. M., "Effect of Nonunity Lewis Number and Finite-Rate Chemistry on the Dynamics of a Hydrogen-Air Jet Diffusion Flame," *Combustion and Flame*, Vol. 96, Nos. 1, 2, 1994, pp. 60–74.

[9] Takagi, T., and Xu, Z., "Numerical Analysis of Laminar Diffusion Flames—Effects of Preferential Diffusion of Heat and Species," *Combustion and Flame*, Vol. 96, Nos. 1, 2, 1994, pp. 50–59.

[10] Smooke, M. D., "Numerical Modeling of Laminar Diffusion Flames," *Numerical Approaches to Combustion Modeling*, edited by E. S. Oran and J. P. Boris, Vol. 135, Progress in Astronautics and Aeronautics, AIAA, Washington, DC, 1991, pp. 183–223.

[11] Takagi, T., Yoshikawa, Y., Yoshida, K., Komiyama, M., and Kinoshita, S., "Studies on Strained Nonpremixed Flames Affected by Flame Curvature and Preferential Diffusion," *26th Symposium (International) on Combustion*, Combustion Inst., Pittsburgh, PA, 1996, pp. 1103–1110.

[12] Takahashi, F., and Schmoll, W. J., "Lifting Criteria of Jet Diffusion Flames," *Twenty-Third Symposium (International) on Combustion*, Combustion Inst., Pittsburgh, PA, 1991, p. 677.

[13] Hsu, K. Y., Chen, L.-D., Katta, V. R., Goss, L. P., and Roquemore, W. M., "Experimental and Numerical Investigations of the Vortex-Flame Interactions in a Driven Jet Diffusion Flame," AIAA Paper 93-0455, Jan. 1993.

[14] Law, C. K., "Heat and Mass Transfer in Combustion: Fundamental Concepts and Analytical Techniques," *Progress in Energy and Combustion Sciences*, Vol. 10, No. 3, 1984, pp. 295–318.

[15] Katta, V. R., Goss, L. P., Roquemore, W. M., and Chen, L. D., "Dynamics of Propane Jet Diffusion Flames," *Atlas of Flow Visualization*, Vol. 3, CRC Press, New York, 1997, pp. 181–198.

[16] Takahashi, F., and Katta, V. R., "Unsteady Extinction Mechanisms of Diffusion Flames," *26th Symposium (International) on Combustion*, Combustion Inst., Pittsburgh, PA, 1996, pp. 1151–1160.

[17] Katta, V. R., Goss, L. P., and Roquemore, W. M., "Numerical Investigations of Transitional H_2/N_2 Jet Diffusion Flames," *AIAA Journal*, Vol. 32, No. 1, 1994, pp. 84–94.

[18] Katta, V. R., and Roquemore, W. M., "On the Structure of Stretched/Compressed Laminar Flamelet—Influence of Preferential Diffusion," *Combustion and Flame*, Vol. 100, No. 1, 1995, p. 61.

[19] Leonard, B. P., "A Stable and Accurate Convective Modeling Procedure Based on Quadratic Upstream Interpolation," *Computer Methods in Applied Mechanics and Engineering*, Vol. 19, No. 1, 1979, pp. 59–98.

[20] Spalding, D. B., "A Novel Finite Difference Formulation for Difference Expressions Involving Both First and Second Derivatives," *International Journal of Numerical Methods in Engineering*, Vol. 4, 1972, p. 551.

[21] Peters, N., "Flame Calculations with Reduced Mechanisms—An Outline," *Reduced Kinetic Mechanisms for Applications in Combustion Systems*, Lecture Notes in Physics, Springer–Verlag, New York, 1993, pp. 3–14.

[22] Frenklach, M., Wang, H., Goldenberg, M., Smith, G. P., Golden, D. M., Bowman, C. T., Hanson, R. K., Gardiner, W. C., and Lissianski, V., "GRI-Mech—An Optimized Detailed Chemical Reaction Mechanism for Methane Combustion," Gas Research Inst., TR GRI-95/0058, Chicago, IL, Nov. 1995.

[23] Hirschfelder, J. O., Curtiss, C. F., and Bird, R. B., *Molecular Theory of Gases and Liquids*, Wiley, New York, 1954, Chaps. 8, 9.

[24] Williams, F. A., *Combustion Theory—The Fundamentals of Chemically Reacting Flow Systems*, Addison–Wesley, Reading, MA, 1985, Appendix E.

[25] Katta, V. R., Goss, L. P., and Roquemore, W. M., "Simulation of Vortical Structures in a Jet Diffusion Flame," *International Journal of Numerical Methods for Heat and Fluid Flow*, Vol. 4, No. 5, 1994, p. 413.

[26] Peters, N., "Numerical and Asymptotic Analysis of Systematically Reduced Reaction Schemes for Hydrocarbon Flames," *Numerical Simulation of Combustion Phenomena*, edited by R. Glowinski, B. Larrouturou, and R. Temam, Vol. 241, Lecture Notes in Physics, Springer–Verlag, Berlin, 1985, p. 90.

[27] Smooke, M. D. (ed.), *Reduced Kinetic Mechanisms and Asymptotic Approximations for Methane–Air Flames*, Springer–Verlag, Berlin, 1991.

[28] Kee, R. J., Miller, J. A., Evans, G. H., and Dixon-Lewis, G., "A Computational Model of the Structure and Extinction of Strained Opposed Flow Premixed Methane-Air Flames," *22nd Symposium (International) on Combustion*, Combustion Inst., Pittsburgh, PA, 1988, pp. 1479–1494.

[29] Warnatz, J., *Combustion Chemistry*, edited by W. C. Gardiner, Springer–Verlag, New York, 1984, p. 197.

[30] Katta, V. R., and Roquemore, W. M., "Extinction in Methane-Air Counterflow Diffusion Flame—A Direct Numerical Study," *Combustion Fundamentals and Applications*, Combustion Inst., Pittsburgh, PA, 1996, pp. 449–454.

[31] Mitchell, R. E., Sarofim, A. F., and Clomburg, L. A., "Experimental and Numerical Investigation of Confined Laminar Diffusion Flames," *Combustion and Flame*, Vol. 37, No. 3, 1980, pp. 227–244.

[32] Davis, R. W., Moore, E. F., Roquemore, W. M., Chen, L.-D., Vilimpoc, V., and Goss, L. P., "Preliminary Results of a Numerical-Experimental Study of the Dynamic Structure of a Buoyant Jet Diffusion Flame," *Combustion and Flame*, Vol. 83, No. 3/4, 1991, pp. 263–270.

[33] Roquemore, W. M., Chen, L.-D., Goss, L. P., and Lynn, W. F., "Structure of Jet Diffusion Flames," *Turbulent Reactive Flows*, Vol. 40, Lecture Notes in Engineering, Springer–Verlag, Berlin, 1988, pp. 49–63.

[34] Eickhoff, H., and Winandy, A., "Visualization of Vortex Formation in Jet Diffusion Flames," *Combustion and Flame*, Vol. 60, No. 1, 1985, pp. 99–101.

[35] Nandula, S. P., Brown, T. M., and Pitz, R. W., "Measurements of Scalar Dissipation in the Reaction Zones of Turbulent Nonpremixed H_2-Air Flames," *Combustion and Flame*, Vol. 99, No. 3/4, 1994, p. 445.

K. Kailasanath
Associate Editor